



**HAL**  
open science

# Martian Ozone Observed by TGO/NOMAD-UVIS Solar Occultation: An Inter-Comparison of Three Retrieval Methods

Arianna Piccialli, Ann Carine Vandaele, Y. Willame, Anni Määttänen, Loic Trompet, J. T. Erwin, F. Daerden, L. Neary, S. Aoki, S. Viscardy, et al.

## ► To cite this version:

Arianna Piccialli, Ann Carine Vandaele, Y. Willame, Anni Määttänen, Loic Trompet, et al.. Martian Ozone Observed by TGO/NOMAD-UVIS Solar Occultation: An Inter-Comparison of Three Retrieval Methods. *Earth and Space Science*, 2023, 10 (2), pp.e2022EA002429. 10.1029/2022ea002429 . insu-04000534

**HAL Id: insu-04000534**

**<https://insu.hal.science/insu-04000534>**

Submitted on 22 Feb 2023

**HAL** is a multi-disciplinary open access archive for the deposit and dissemination of scientific research documents, whether they are published or not. The documents may come from teaching and research institutions in France or abroad, or from public or private research centers.

L'archive ouverte pluridisciplinaire **HAL**, est destinée au dépôt et à la diffusion de documents scientifiques de niveau recherche, publiés ou non, émanant des établissements d'enseignement et de recherche français ou étrangers, des laboratoires publics ou privés.



Distributed under a Creative Commons Attribution - NonCommercial - NoDerivatives 4.0 International License

# Earth and Space Science

















## RESEARCH ARTICLE

10.1029/2022EA002429

# Martian Ozone Observed by TGO/NOMAD-UVIS Solar Occultation: An Inter-Comparison of Three Retrieval Methods

### Key Points:

- We compare three different retrieval codes and different criteria to filter spurious detection of ozone on Mars
- The filtering criteria demonstrate the ozone detection in perihelion season is mostly spurious in both years
- The three retrieval methods produce consistent results with a maximum percentage difference of ~30% for large ozone densities below 50 km

A. Piccialli<sup>1</sup> , A. C. Vandaele<sup>1</sup> , Y. Willame<sup>1</sup>, A. Määttänen<sup>2</sup> , L. Trompet<sup>1</sup> , J. T. Erwin<sup>1</sup>, F. Daerden<sup>1</sup> , L. Neary<sup>1</sup> , S. Aoki<sup>1,3</sup> , S. Viscardy<sup>1</sup> , I. R. Thomas<sup>1</sup> , C. Depiesse<sup>1</sup> , B. Ristic<sup>1</sup> , J. P. Mason<sup>3</sup>, M. R. Patel<sup>3,4</sup> , M. J. Wolff<sup>5</sup> , A. S. J. Khayat<sup>6</sup> , G. Bellucci<sup>7</sup>, and J.-J. Lopez-Moreno<sup>8</sup>

<sup>1</sup>Planetary Aeronomy, Royal Belgian Institute for Space Aeronomy, Brussels, Belgium, <sup>2</sup>LATMOS/IPSL, Sorbonne Université, UVSQ, CNRS, Paris, France, <sup>3</sup>Graduate School of Frontier Sciences, The University of Tokyo, Kashiwa, Japan, <sup>4</sup>School of Physical Sciences, The Open University, Milton Keynes, UK, <sup>5</sup>Space Science and Technology Department, Science and Technology Facilities Council, Rutherford Appleton Laboratory, Oxfordshire, UK, <sup>6</sup>Planetary Systems Laboratory, Solar System Exploration Division, NASA Goddard Space Flight Center, Greenbelt, MD, USA, <sup>7</sup>Istituto di Astrofisica e Planetologia Spaziali, IAPS-INAF, Rome, Italy, <sup>8</sup>Instituto de Astrofisica de Andalucia, IAA-CSIC, Granada, Spain

### Supporting Information:

Supporting Information may be found in the online version of this article.

### Correspondence to:

A. Piccialli,  
arianna.piccialli@aeronomie.be

### Citation:

Piccialli, A., Vandaele, A. C., Willame, Y., Määttänen, A., Trompet, L., Erwin, J. T., et al. (2023). Martian ozone observed by TGO/NOMAD-UVIS solar occultation: An inter-comparison of three retrieval methods. *Earth and Space Science*, 10, e2022EA002429. <https://doi.org/10.1029/2022EA002429>

Received 16 MAY 2022

Accepted 7 DEC 2022

### Author Contributions:

**Conceptualization:** A. Piccialli, F. Daerden, L. Neary, S. Aoki, S. Viscardy, M. R. Patel, M. J. Wolff, A. S. J. Khayat, G. Bellucci, J.-J. Lopez-Moreno  
**Data curation:** Y. Willame, L. Trompet, J. T. Erwin, F. Daerden, S. Aoki, I. R. Thomas, C. Depiesse, B. Ristic, J. P. Mason  
**Formal analysis:** A. Piccialli  
**Funding acquisition:** A. C. Vandaele  
**Investigation:** A. Piccialli, L. Neary

**Abstract** The NOMAD-UVIS instrument on board the ExoMars Trace Gas Orbiter has been investigating the Martian atmosphere with the occultation technique since April 2018. Here, we analyze almost two Mars Years of ozone vertical distributions acquired at the day-night terminator. The ozone retrievals proved more difficult than expected due to spurious detections of ozone caused by instrumental effects, high dust content, and very low values of ozone. This led us to compare the results from three different retrieval approaches: (a) an onion peeling method, (b) a full occultation Optimal Estimation Method, and (c) a direct onion peeling method. The three methods produce consistently similar results, especially where ozone densities are higher. The main challenge was to find reliable criteria to exclude spurious detections of O<sub>3</sub>, and we finally adopted two criteria for filtering: (a) a detection limit, and (b) the  $\Delta\chi^2$  criterion. Both criteria exclude spurious O<sub>3</sub> values especially near the perihelion ( $180^\circ < L_s < 340^\circ$ ), where up to 98% of ozone detections are filtered out, in agreement with general circulation models, that expect very low values of ozone in this season. Our agrees well with published analysis of the NOMAD-UVIS data set, as we confirm the main features observed previously, that is, the high-altitude ozone peak around 40 km at high latitudes. The filtering approaches are in good agreement with those implemented for the SPICAM/ME<sub>x</sub> observations and underline the need to evaluate carefully the quality of ozone retrievals in occultations.

## 1. Introduction

Since its discovery on Mars in the early 1970s (Barth & Hord, 1971; Barth et al., 1973), O<sub>3</sub> has been characterized by a large variety of observations acquired by ground-based instruments (Fast et al., 2006), the Hubble Space Telescope (Clancy et al., 1999), and satellite instruments (Clancy et al., 2017; Gröller et al., 2018; Lebonnois et al., 2006; Willame et al., 2017).

Stellar and solar occultations in the ultraviolet provided initially the only vertical profiles of Martian ozone (Daerden, Neary, Villanueva, et al., 2022; Daerden, Neary, Wolff, et al., 2022; Khayat et al., 2021; Lebonnois et al., 2006; Montmessin et al., 2011; Patel, Mason, et al., 2021; Patel, Sellers, et al., 2021; Piccialli et al., 2021). Recently, the mid-infrared channel of the Atmospheric Chemistry Suite (ACS MIR) on board the ExoMars TGO allowed investigation of the O<sub>3</sub> vertical structure (Olsen et al., 2022).

The ultraviolet spectral region is affected both by ozone and aerosols. Whilst the Hartley absorption band of ozone is clearly visible around 250 nm, the aerosols affect the entire spectral range by attenuating the spectrum in a uniform way (Määttänen et al., 2013; Montmessin et al., 2006).

Aerosols are ubiquitous on Mars, usually forming a thin, reddish veil covering the planet. During storms, even surface features cannot be distinguished any longer. Clouds, together with dusty aerosols, can strongly affect the spectral range between 200–600 nm. This effect is expected to be most significant during aphelion (Clancy et al., 1996) and in particular during dust storms. The retrieval of ozone is strongly influenced by the aerosols presence and high quantities of dust in the atmospheres can make the retrieval of ozone challenging, if not

© 2023 The Authors. Earth and Space Science published by Wiley Periodicals LLC on behalf of American Geophysical Union.

This is an open access article under the terms of the [Creative Commons Attribution-NonCommercial-NoDerivs License](https://creativecommons.org/licenses/by/4.0/), which permits use and distribution in any medium, provided the original work is properly cited, the use is non-commercial and no modifications or adaptations are made.

**Methodology:** A. Piccialli, A. C. Vandaele, A. Määttänen, L. Trompet, J. T. Erwin, I. R. Thomas, A. S. J. Khayat  
**Project Administration:** A. C. Vandaele  
**Resources:** Y. Willame, L. Trompet, J. T. Erwin, F. Daerden, L. Neary, S. Aoki, S. Viscardy, I. R. Thomas, C. Depiesse, B. Ristic, J. P. Mason, M. R. Patel  
**Software:** A. Piccialli, A. C. Vandaele, L. Trompet, J. T. Erwin, I. R. Thomas  
**Supervision:** A. C. Vandaele  
**Validation:** A. Piccialli, Y. Willame, A. Määttänen, L. Trompet, F. Daerden, M. J. Wolff, A. S. J. Khayat  
**Visualization:** A. Piccialli, F. Daerden, I. R. Thomas  
**Writing – original draft:** A. Piccialli  
**Writing – review & editing:** A. Piccialli, A. C. Vandaele, A. Määttänen, I. R. Thomas, J. P. Mason, M. R. Patel, M. J. Wolff, A. S. J. Khayat

impossible, for both nadir and solar occultations (Määttänen et al., 2022; Willame et al., 2017). Low ozone quantities, high dust content in the atmosphere, and instrumental effects may result in convergence to a solution that is heavily biased by the a priori, provide results with large errors, or give unrealistic high values of ozone.

It is therefore necessary to establish appropriate criteria to validate the detection of ozone in the Martian atmosphere and to filter spurious detections, as recently proposed for SPICAM ozone data by Määttänen et al. (2022), and by Daerden, Neary, Villanueva, et al. (2022), Daerden, Neary, Wolff, et al. (2022) on a selected sample of the NOMAD-UVIS data set. Multiple retrieval methods, and various approaches to error estimation, can be used on observations from remote sensing instruments. The choice of a specific method may depend on different factors (i.e., computation time, flexibility, ease of use, etc.). Surely, one of the advantages of having a variety of spectral retrieval approaches is that each retrieval code may be particularly suited for a specific scenario (i.e., cloud parametrization, 3D modeling, different geometry of observations, etc.). Moreover, while all the models follow approximately the same basic structure, different approaches may lead to different solutions for the same data set. Having a diversity of retrieval codes, with different peculiarities, gives the possibility to identify the differences between the models and to evaluate their impact on the retrievals. In addition, each retrieval scheme provides different tools that may be of help to discriminate spurious detections.

In this work, we present a comparison of three different retrieval codes for the analysis of ozone observed with the NOMAD-UVIS instrument on board the ExoMars Trace Gas Orbiter (TGO). We analyzed the data set already introduced in Patel, Mason, et al. (2021), Patel, Sellers, et al. (2021), Khayat et al. (2021), acquired between April 2018 (MY 34,  $L_s = 163^\circ$ ) and November 2020 (MY 35,  $L_s = 320^\circ$ ), and we extended it to November 2021 (MY 36,  $L_s = 132^\circ$ ). In total, this data set comprises more than 8,300 solar occultations. We compare: (a) an onion peeling method (OP), (b) a full occultation Optimal Estimation Method (FOEM), and (c) a direct onion peeling method (DOP). The OP method is similar to that used for Mars and Venus stellar occultations (Gröller et al., 2018; Piccialli et al., 2015; Quémerais et al., 2006). The FOEM and DOP approaches are based on ASIMUT-ALVL, the BIRA-IASB radiative code (Vandaele et al., 2006). This is a modular program initially developed for Earth observations missions, and then implemented for planetary atmospheres, such as Venus (Vandaele et al., 2008) and Mars (Piccialli et al., 2021; Vandaele et al., 2018).

We describe the NOMAD-UVIS data set in Section 2. We provide details for the three retrieval tools used in this work in Section 3 and then present the retrieval comparison in Section 4. In Section 4.2, we compare the filtering approaches applied to NOMAD-UVIS and SPICAM-UV ozone retrievals.

## 2. Observations: NOMAD-UVIS Solar Occultations

### 2.1. The Instrument: NOMAD-UVIS

The NOMAD (Nadir and Occultation for MArS Discovery) instrument—operating on board the ExoMars 2016 Trace Gas Orbiter (TGO) mission—started to acquire the first scientific measurements on 21 April 2018.

NOMAD is a spectrometer composed of three channels: (a) a solar occultation channel (SO) operating in the infrared (2.3–4.3  $\mu\text{m}$ ); (b) the Limb, Nadir and Occultation channel (LNO), capable of doing nadir, as well as solar occultation and limb observations in the infrared (2.3–3.8  $\mu\text{m}$ ); and (c) the Ultraviolet and VISible spectrometer (UVIS) (200–650 nm) that can also observe in all three observation modes (Neefs et al., 2015; Vandaele et al., 2015).

The UVIS channel has a spectral resolution of 1.2–1.6 nm. The UVIS detector is a CCD with 256 rows (spatial direction) of 1,024 pixels along the spectral direction. A detailed description of the instrument as well as its scientific objectives can be found in Patel et al. (2017), Patel, Mason, et al. (2021), Patel, Sellers, et al. (2021), Khayat et al. (2021). In the solar occultation mode, it is mainly devoted to study the climatology of ozone and aerosol content.

### 2.2. UVIS Solar Occultation Data Set

For this study we analyzed data from 8,317 solar occultations acquired by UVIS between April 2018 and November 2021, which cover more than one Martian year and a half (MY 34,  $LS = 163^\circ$  to MY 36,  $LS = 132^\circ$ ). Figure 1 shows the seasonal and latitudinal coverage of the solar occultations used for this study.

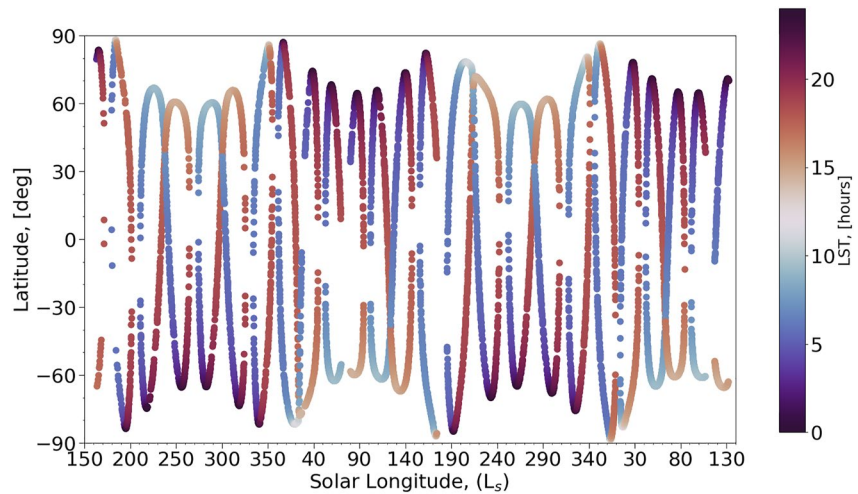


**Figure 1.** Solar longitude ( $L_s$ ) and latitude of the solar occultation measurements acquired from April 2018 to November 2021 by TGO/NOMAD-UVIS and used in this study. The colors indicate the local solar time (LST) of observations.

While observations have a good latitudinal coverage, there is a better sampling of observations at higher latitudes due to the geometry of the orbit. It is important to note that solar occultations probe the atmosphere exclusively at the day-night terminator.

A solar occultation profile presents a slanted vertical path, which corresponds to a latitudinal/longitudinal range of  $<1^\circ$  at higher latitudes up to  $<10^\circ$  around the equator.

In the initial phase of the science mission ( $L_s = 163\text{--}345^\circ$ ), the vertical resolution varied between 0.7 and 4.4 km. After  $L_s = 345^\circ$  (MY 34), the vertical resolution was improved, reaching values in the range 0.2–1.4 km (see also Patel, Mason, et al. (2021); Patel, Sellers, et al. (2021) for additional details).

### 2.3. Calibration

UVIS raw data requires several corrections before being useable for a proper transmittance calculation. A complete description of the calibration process can be found in Willame et al. (2022) and Mason et al. (2022). First, the dark current (DC) has to be removed: the DC is estimated from a temperature dependent interpolation between the two dark measurements recorded at the beginning and end of each occultation. Second, a noise removal algorithm is applied in order to remove anomalous pixels and cosmic rays to obtain a clean CCD frame. Finally, the UVIS data suffer from straylight contamination. The straylight, coming from the UVIS range itself but also from the near infrared, has to be removed: the straylight in the illuminated region at the center of the CCD is estimated using an interpolation from the non-illuminated parts lying at the top and bottom of the CCD where only straylight is present (Willame et al., 2022).

### 2.4. Transmittance Estimation

The transmittance calibration is based on Trompet et al. (2016) and further improved in Trompet et al. (2023) for NOMAD occultation spectra. The spectra recorded as an occultation are split in three main regions: The Sun region (S) when UVIS points to the Sun and no atmospheric absorption is present, the atmospheric region (A) where UVIS line of sight crosses the atmosphere, and the Umbra region (U) when UVIS line of sight crosses the planet. For UVIS, the limit between the regions S and A is always 120 km. Two examples of the variation of the signal along an occultation are represented in Figure 2. We compute the transmittance spectra as the ratio of the atmospheric spectra divided by a Sun reference spectrum. For this work, we do not compute the Sun reference spectrum as in Trompet et al. (2016) but simply compute an average spectrum in S. Nevertheless, as in Trompet et al. (2016), we do not necessarily consider the whole Sun region as some unexpected events might modify the signal. An example is given in Figure 2(right) where, for this occultation, the high gain antenna of TGO moved (at a corresponding tangent altitude of 230 km) and the UVIS pointing was affected by a limb darkening.

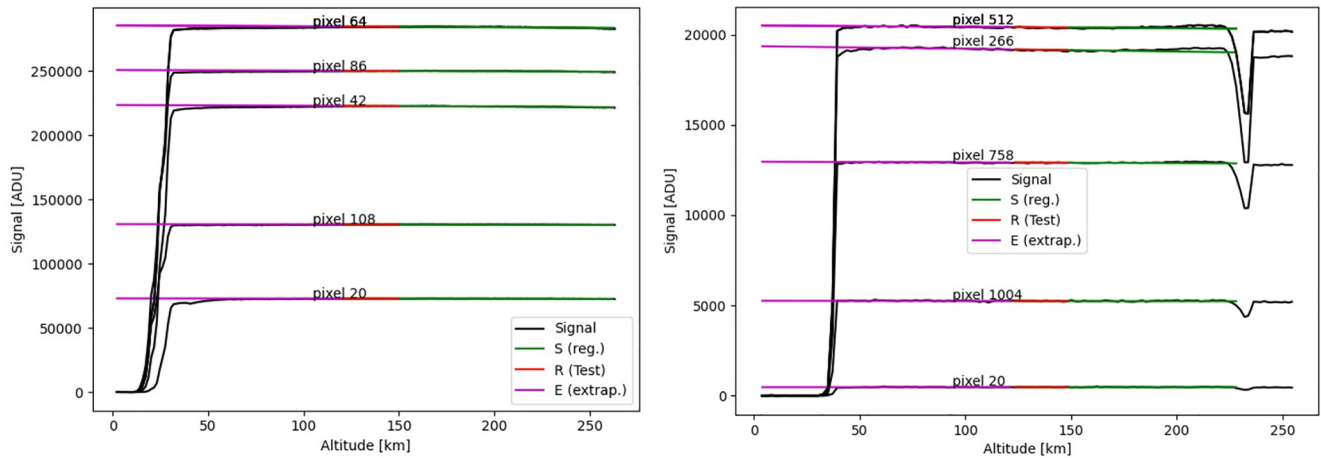


**Figure 2.** Example of variation of the signal over six pixels chosen along the spectral direction on the UVIS detector for two different occultations. Each pixel corresponds to one wavelength. The selected Sun region is in green and red, and the atmospheric region is in purple. The red line is the region where a test is made by the algorithm selecting the Sun region (details in Trompet et al. (2016)).

We forward propagate the uncertainties  $\delta T$  on the transmittance  $T$  by quadrature over the atmospheric spectrum  $A$ , and the Sun reference spectrum  $\hat{S}$  as:

$$\delta T = T \sqrt{\left(\frac{\delta A}{A}\right)^2 + \left(\frac{\delta S}{S}\right)^2} \quad (1)$$

and where  $\delta A$  and  $\delta S$  are their corresponding uncertainties. We compute the uncertainties  $\delta A$  as the standard deviation on the signal in count and over the pixels interpolated from  $S$  to  $U$  and  $\delta \hat{S}$  is the standard deviation over the spectra in  $S$  computed for each pixel.

Average transmission values in the spectral range 240–293 nm below 0.07 are not considered in the retrieval process, since the signal on the CCD detector becomes comparable to the noise. The signal-to-noise ratio (SNR) in the transmittance varies with the altitude, the wavelength and the observation. As an example, the occultation used in Figure 3 has an average SNR of  $\sim 730$  at 65 km and of  $\sim 580$  at 22 km in the spectral range 300–330 nm.

### 3. Data Analysis: An Inter-Comparison of Three Retrieval Methods

In this section we review the results of three retrieval schemes, along with related error estimation: (a) a onion peeling scheme (OP); (b) a full radiative transfer model (ASIMUT); and (c) a direct onion peeling method (DOP).

#### 3.1. Input Atmospheric Profiles From the GEM-Mars General Circulation Model

For the atmospheric input profiles, we use the GEM-Mars Global Climate Model (GCM) with online chemistry. The simulations used are presented and described in Daerden, Neary, Villanueva, et al. (2022), Daerden, Neary, Wolff, et al. (2022), and in Daerden et al. (2019) for the description of the chemistry part of the model. These have a horizontal resolution of  $4^\circ \times 4^\circ$  with a time step of 1/48th of a Mars solar day or sol. Every 10 Ls, one full sol (output every time step) is provided so that the model seasonal and diurnal cycles are represented. The dust optical depths are scaled to the climatology of Montabone et al. (2015, 2020).

#### 3.2. Information Common to All Retrieval Methods

The spectral range used in the retrieval is 240–330 nm. We chose this spectral range to avoid the straylight contamination at wavelengths  $< 220$  nm. For a more detailed discussion about the straylight contamination see Willame et al. (2022). It shows a clear absorption feature of  $O_3$  at 250 nm, while the extinction due to aerosols affects the entire spectral range.  $CO_2$  absorption becomes negligible above 180 nm.

In order to fit the transmission spectra, we must know the absorption cross sections of the absorbing species. We selected the cross-sections from Huestis and Berkowitz (2010) for  $CO_2$ , since they cover a wide spectral

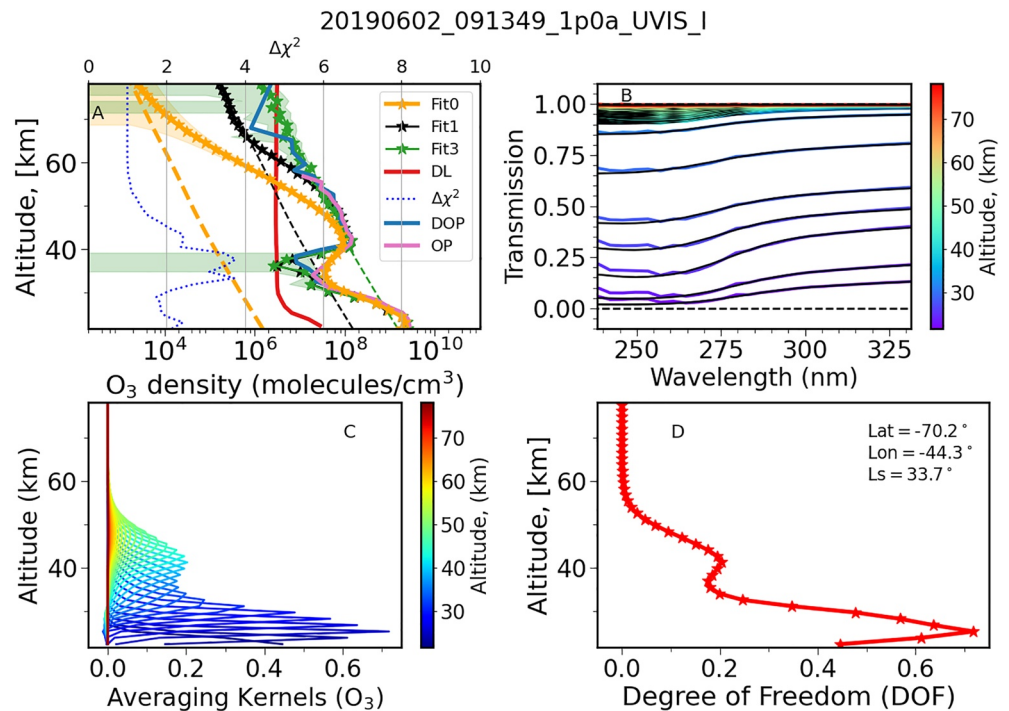


**Figure 3.** (a) Retrieved ozone profiles (solid lines) with the FOEM method (yellow, black, green lines) starting from different a priori profiles (dashed lines). DOP and OP retrievals are displayed as blue and pink lines. The ozone Detection Limit (red line) and the  $\Delta\chi^2$  (dot blue line) are also shown. (b) Example of UVIS transmission spectra at different altitudes: (blue) low altitudes; (red) high altitudes. Black lines are fitted spectra calculated using the FOEM method. (c) Averaging kernels. (d) Degree of Freedom.

interval at high resolution. Moreover, they are in very good agreement with the data of Parkinson et al. (2003) obtained at 295 K. We built the O<sub>3</sub> cross-sections around the temperature dependent data sets of Serdyuchenko et al. (2014), and we extended the cross sections toward shorter wavelengths by using either the Reims data set (Brion et al., 1993; Daumont et al., 1992; Malicet et al., 1995) or the JPL compilation (Sander et al., 2011) depending on the available temperatures. From this data, we implemented temperature-dependent cross-sections for O<sub>3</sub> which were used to calculate the optical depth at the temperature of any layer.

The above mentioned algorithms typically assume that the atmosphere is horizontally homogeneous, which is not completely fulfilled at the terminator for ozone, a photochemically active species. Ignoring horizontal gradients along the line of sight can cause an error of about 20%, although this may depend on the inputs from the GCM (see Piccialli et al. (2021) for details). We plan to investigate the effect of horizontally inhomogeneous species along the line-of-sight in a future article focusing on NOMAD observations.

### 3.3. Onion Peeling Scheme (OP)

Using the same retrieval method as in Quémerais et al. (2006), Montmessin et al. (2006), Piccialli et al. (2015), Gröller et al. (2018), Patel, Mason, et al. (2021), Patel, Sellers, et al. (2021), Khayat et al. (2021), Daerden, Neary, Villanueva, et al. (2022), Daerden, Neary, Wolff, et al. (2022), we retrieved line-of-sight integrated densities (slant densities) for O<sub>3</sub> and aerosols, from which local densities were later obtained. For a complete description of the analysis method, we invite the reader to refer to the above cited papers, here we will only focus on specific aspects relevant to this study.

As a first step, we fitted the transmission spectra using the Beer-Lambert law by taking in account the gaseous species (CO<sub>2</sub> and O<sub>3</sub>), as well as the aerosol extinction due to composition and particle size distribution.

The aerosol optical thickness is approximated using the  $\alpha$ -formalism, first used to model the dust behavior on Earth, and then applied on Mars (Dubovik et al., 2000; Määttänen et al., 2013; Montmessin et al., 2006):

$$\tau_\lambda = \tau_{\lambda_0} (\lambda/\lambda_0)^\alpha \quad (2)$$

where  $\lambda$  is the wavelength in nanometers,  $\tau_{\lambda_0}$  the aerosol slant opacity at the reference wavelength  $\lambda_0$  (here taken at 250 nm). The exponent  $\alpha$ —referred to as the Ångström coefficient—describes the spectral dependence of aerosol extinction.

Each spectrum is fitted using a Levenberg-Marquardt algorithm, where  $O_3$ ,  $\tau_{\lambda_0}$ , and  $\alpha$  are the free parameters. As input parameters,  $CO_2$ , temperature and pressure vertical profiles are taken from the GEM-Mars simulations. Uncertainties for the slant densities are a by-product of the Levenberg-Marquardt routine, being obtained as the square root of the diagonal terms of the returned covariance matrix.

In the vertical inversion, quantities integrated along the line-of-sight are transformed to local densities with an onion-peeling method as described in Quémerais et al. (2006). From the vertical inversion, we obtained local  $O_3$  densities, the aerosol extinction coefficient, and the Ångström coefficient. Figure 3a shows an example of an OP retrieval (pink line), compared to profiles derived from the other two methods.

### 3.4. Full Occultation Optimal Estimation Method (FOEM)

Ozone retrievals were performed using the ASIMUT-ALVL radiative code developed at IASB-BIRA (Vandaele et al., 2006). A detailed description of the retrieval method can be found in Piccialli et al. (2021).

In this method, ASIMUT analyzes simultaneously all transmittances within a solar occultation at the various tangent heights, eventually deriving a single  $O_3$  profile to best fit the ensemble of spectra.

We divided the atmosphere in layers whose boundaries were the different tangent altitudes of the observation, adding a single layer of 5 km width above the highest tangent height up to 120 km, which was considered the upper limit. Aerosols were not taken in account into the retrieval procedure. ASIMUT, in fact, enables the user to fit the baseline spectrum. By configuring this additional fit, we could reduce the impact caused by the uncertainties concerning the aerosols.

Several input parameters are needed to constrain the retrieval: a priori vertical profiles of the different species included ( $CO_2$  and  $O_3$ ) as well as of the temperature and pressure of the atmosphere. All a priori information is taken from the GEM-Mars simulations. We assumed as an a priori nominal ozone profile a constant value of 0.1 ppb.

First, we tested the dependency of ozone retrievals to the choice of the ozone a priori profile. Following the same approach of Irwin et al. (2008), we tested a range of a priori errors to obtain a solution that is equally constrained by the a priori profile and by the data.

In Figure 3a, as an example, we show the retrieval of the occultation #20190602\_091349\_1p0a\_UVIS\_I. We used as a priori profiles three constant VMR profiles, respectively: (Fit0) 0.1 ppb; (Fit1) 10 ppb; and (Fit3) 100 ppb. In all cases, the retrieved profiles converge within errors below  $\sim 45$  km.

In addition to the retrieved ozone profiles, ASIMUT produces several metrics that can be used to assess the retrievals. In this study we tested: (a) the ozone detection limit (DL), red line in Figure 3a; (b) the averaging kernels (AK), Figure 3c; (c) the Degree of Freedom (DoF), Figure 3d; and (d) the  $\Delta\chi^2$ , blue dotted line in Figure 3a. We will describe them in more detail in Section 3.6.

### 3.5. Direct Onion Peeling Method (DOP)

Another method has been implemented into ASIMUT that is based on the onion peeling technique, but directly producing local abundances instead of slant column abundances which need a vertical inversion to obtain the local densities as is done in the OP method (see Section 3.3). In this method, each transmittance is treated separately. We start from the uppermost layer, and sequentially go down through the atmosphere, to reconstruct the vertical profiles of the fitted parameters step-by-step.

For the first layer (i.e., the highest), the equation to solve is simply:

$$y_{layer1} = \exp(-n_{O_3,layer1} \cdot d_{layer1} \cdot \sigma_{O_3,layer1}) \quad (3)$$

considering for the sake of clarity that only the ozone abundance is fitted. In this equation,  $y_{layer1}$  is the transmittance of the first top layer,  $n_{O_3,layer1}$  is the ozone abundance in that layer,  $d_{layer1}$  is the light path length through

the layer considering the geometry corresponding to the transmittance 1, and  $\sigma_{O_3,layer1}$  is the absorption cross section of ozone (calculated at the temperature of *layer1*). Although this expression is quite simple to invert, we nevertheless use the OEM formalism implemented into ASIMUT, because this method provides several metrics to assess the quality of the fit (see Section 3.6). Solving Equation 3 using a simple Singular Value Decomposition (svd) method provides the initial values of the fitted parameters, which is fed into the OEM method as a priori.

For the next layers, we consider the values of all fitted parameters in the previous steps to calculate the contribution of the layers lying above the most internal layer:

$$y_{layer_i} = \exp(-n_{O_3,layer_i} \cdot d_{layer_i} \cdot \sigma_{O_3,layer_i}) + \exp\left(-\sum_{l=i-1}^1 n_{O_3,l} \cdot d_l \cdot \sigma_{O_3,l}\right) \quad (4)$$

the first term of the right hand side of the equation corresponds to the contribution of the lowest *layer<sub>i</sub>*, while in the second term, all abundances (parameters) are known from the fit of the layers above. Solving this equation gives the ozone abundance (fitted parameters) at layer *i*.

When using the DOP method, the fitted parameters were the ozone abundances, the dust number densities and the Ångström coefficients, and the fit was carried out on the 210–400 nm spectral range, in a two steps procedure: first fitting the dust (number densities and Ångström coefficient) excluding the 221–300 nm region where ozone absorbs, then fitting the ozone density on the full range considering the dust results. The DOP method highly depends on the integrated abundance in the most inner layer, as shown in Equation 4. It provides a solution only if the absorption signature of the fitted parameter exceeds the noise. So for low abundances and/or thin layers, this approach might not be able to derive any Figure 3a shows an example of DOP retrieval (blue line), compared to profiles derived from the other two methods.

### 3.6. Filtering Criteria

In this section, we will review different criteria that can be used to filter spurious detections of ozone: (a) the ozone detection limit (DL), (b) the averaging kernels (AK), (c) the Degree of Freedom (DoF), and (d) the  $\Delta\chi^2$ . Whilst the  $\Delta\chi^2$  and the DL criteria are used for the three retrieval methods, the AK, and the DoF are applied only to the FOEM and DOP approaches. A similar approach to ours was implemented by Daerden, Neary, Villanueva, et al. (2022) and Daerden, Neary, Wolff, et al. (2022) on a selected sample of the NOMAD/UVIS data set, and by Määttä et al. (2022) on SPICAM-UV observations. The application of a criterion, or of a combination of them, needs to be evaluated in a semi-empirical way in order to find a balance between the exclusion of spurious detections retaining at the same time real ones. In the following study, we found that the best approach was to apply a combination of the ozone detection limit (DL) and the  $\Delta\chi^2$  criteria.

#### 3.6.1. Ozone Detection Limit (DL)

We computed the ozone detection limit (DL) for NOMAD-UVIS spectra at each tangent height sounded. The approach is similar to what was done in Trompet et al. (2021) for the Venusian phosphine detection limits with SOIR/VEx. The detection limit at the tangent altitude  $z_{tg}$  is:

$$DL_{z_{tg}} = n(0) \times \ln\left(\frac{Y_{bg}}{Y_{bg} - Y_{Error}}\right) \times \frac{1}{\sigma(255 \text{ nm}) \cdot \int_{z_{tg}}^{z_{top}} n(z) dz} \quad (5)$$

where  $n(z)$  is the density profile at the altitude level  $z$ ,  $\sigma(255 \text{ nm})$  is the absorption cross section of ozone at 255 nm, and  $Y_{Error}$  is the standard deviation of the uncertainties on the transmittances between 240 and 302 nm. Finally,  $Y_{bg}$  is the linear interpolation between 240 and 302 nm, defined as:

$$Y_{bg} = Y(240 \text{ nm}) + \frac{Y(302 \text{ nm}) - Y(240 \text{ nm})}{X(302 \text{ nm}) - X(240 \text{ nm})} \times (X(255 \text{ nm}) - X(240 \text{ nm})) \quad (6)$$

with  $X$  the wavelength.

The detection limit is shown by a red line in Figure 3a. Above ~50 km, the ozone vertical profiles are lower than the DL and therefore will be filtered out.

The impact of applying the DL filter can be seen in Figure 4, where we compare the seasonal evolution of FOEM ozone vertical profiles for different latitude ranges without any filtering (Right panels) with the same profiles



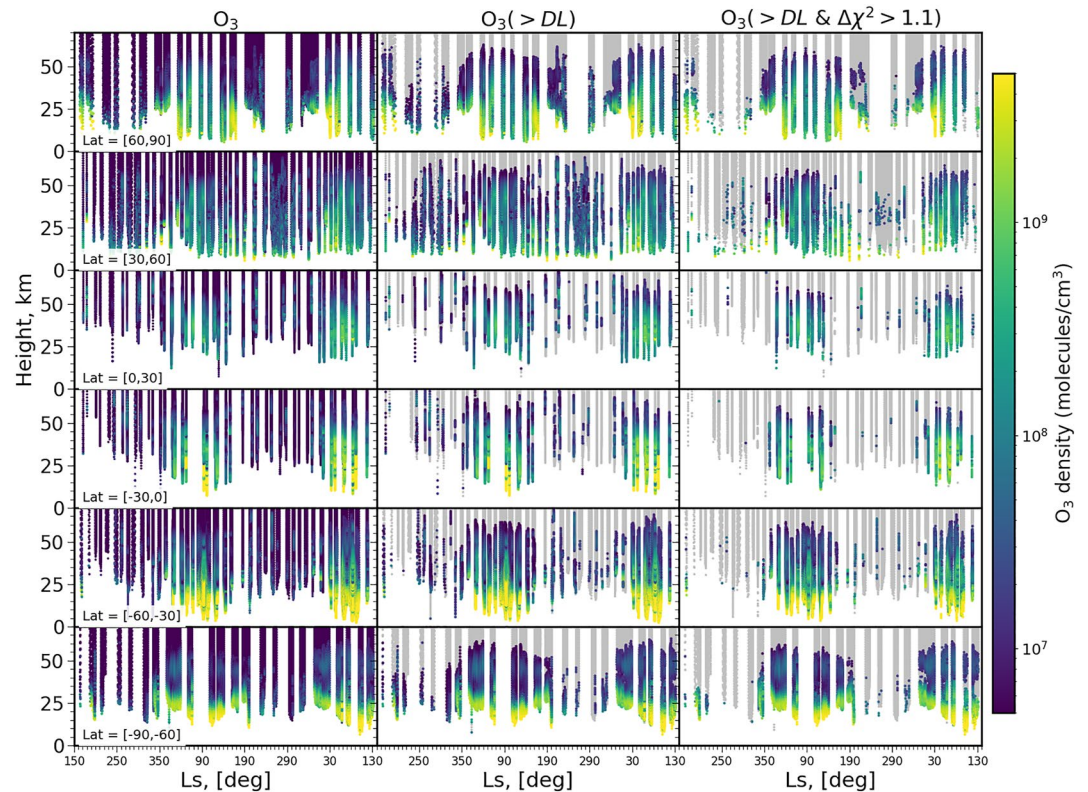


**Figure 4.** Seasonal evolution of FOEM ozone abundance observed by NOMAD-UVIS for different latitude ranges. Left panels show the ozone retrievals without any filtering; in the middle panels we applied the DL filter; and in the right panels we applied both the DL and  $\Delta\chi^2$  filters.

filtered with the DL (Middle panels). This criterion removes up to 72% of ozone detections, depending on the retrieval method (see Table 1), and it eliminates very low values of ozone that do not have physical meaning.

In Figure 5, we present an example of  $O_3$  detection that is filtered out by the DL criterion. The three retrievals do not converge, the FOEM profile is well below the DL, while the DOP and the OP vertical profiles are above the DL. A visual inspection of spectra at different altitudes confirms the lack of  $O_3$ , or values of ozone well below the detection limit of the instrument. For very low values of ozone, or below the DL, the OP profiles generally remain above and close to the DL, or simply fails to converge. In this example, to ensure the correct filtering of the DOP and OP profiles, it is necessary to apply an additional filtering criterion, the  $\Delta\chi^2$  criterion, which will be introduced below.

### 3.6.2. Averaging Kernels (AK)

Averaging kernel functions (AK) allow to study how the information content is distributed in the retrieved profiles (Rodgers, 2000). They provide an estimation of the vertical sensitivity of the retrieval and peak at the altitude of maximum sensitivity.

Figure 3c shows an example of averaging kernels. From this plot it is evident that the information content is constrained to the altitude range  $<50$  km. An alternative representation of the information content, is given by the trace of the AK matrix, defined in the next section.

### 3.6.3. Degree of Freedom (DoF)

The trace of the AK matrix gives the degrees of freedom (DOF), defined as the number of independent pieces of information in the retrieved profile (Note i.e., in fact the degrees of freedom for signal (DOFFS) as defined in

**Table 1**  
DoF and  $\Delta\chi^2$  Threshold Values at 10% for the Three Retrieval Approaches

	FOEM (%)	DOP (%)	OP (%)
DL	(66%)	(72%)	(8%)
DoF	0.2 (80%)	0.7 (88%)	–
$\Delta\chi^2$	1.1 (79%)	4.3 (91%)	3.0 (37%)

*Note.* The percentage of ozone detections filtered out for each criterion is indicated within parenthesis. In the case of the DL, we display only the percentage of excluded  $O_3$ .

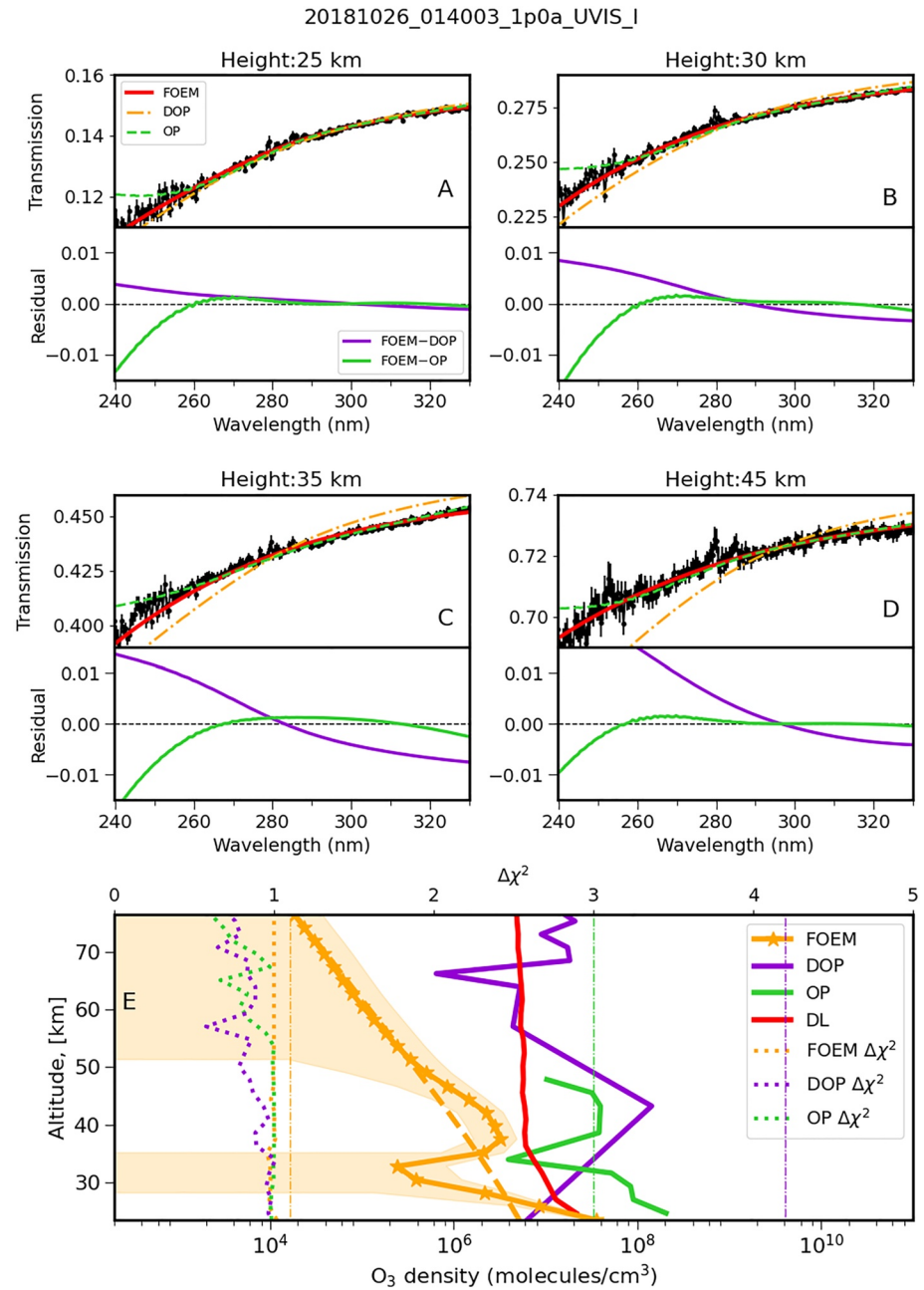


**Figure 5.** (a–d) The top panel shows the spectrum for four different altitudes (black) and the fits for the three retrieval methods. The bottom panel displays the differences between the FOEM method and the DOP and OP methods (violet and green curves, respectively). (e) Retrieved ozone profiles (solid lines) with the FOEM (yellow), DOP (purple), and OP (green) methods. We displayed the DL as a red line. The dashed yellow line is the a priori. The  $\Delta\chi^2$  values and their thresholds (dash-dotted lines) are also shown for the three methods.

Rodgers (2000)). The DoF varies between 0 and 1: A DoF of 1 indicates that the retrieved value of the parameter was entirely deduced from the measurement while a DoF of 0 means that the retrieval was not sensitive to this parameter and the retrieved value comes therefore from the a priori. In Figure 3 (bottom right), the DoF goes to zero at about 50 km, in good agreement with the averaging kernels.

To derive a more precise threshold for the DoF, we selected a sample of occultations without ozone, that is for a null-test set, as in Määttä et al. (2022). We therefore used only observations near the equator (latitude = [−30°, 30°]) and during the perihelion ( $L_s = 240^\circ - 280^\circ$ ). As shown in Figure 6, based on GEM-Mars GCM simulations,

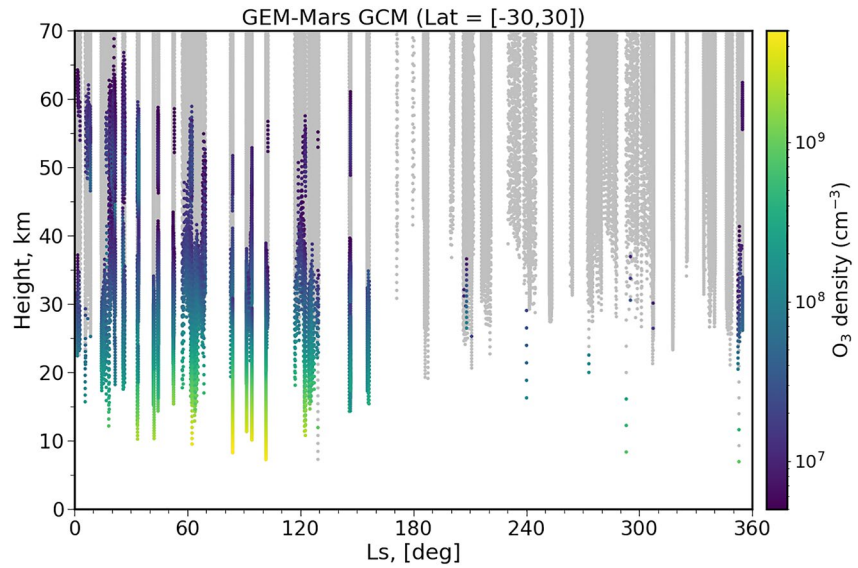


**Figure 6.** GEM-Mars GCM simulations of ozone co-located with NOMAD-UVIS observations at latitudes =  $[-30^\circ, 30^\circ]$ . In gray is shown where  $O_3 < DL$ .

we expect  $O_3$  to be below NOMAD-UVIS detection limits (DL) at these latitudes and Ls. An additional visual inspection of the spectra, as in Määttä et al. (2022), confirmed the absence of  $O_3$  in this sample.

To derive the DoF thresholds, we derived a distribution for the FOEM and DOP methods, as shown in Figure 7. We fitted a  $\chi^2$  distribution to the two cases, considering only  $O_3$  values  $>DL$ . We opted for a threshold of 10% in the null-test sample for the two methods (see Table 1), which means that a DoF  $>$  the threshold has a 10% probability to be a spurious detection within the null-test set. The choice of a 10% threshold was done empirically, we found this to be the best compromise to exclude spurious detections of  $O_3$  in the null-test set, but at the

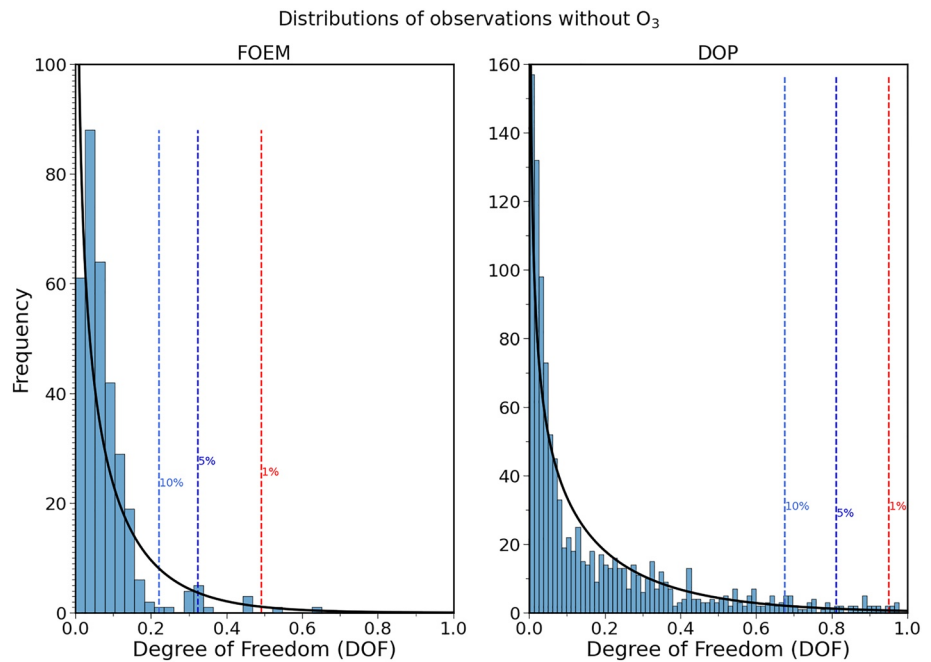


**Figure 7.** Histograms represent the distributions of a sample of occultation without  $O_3$  (null-test sample) for the FOEM and DOP retrieval methods. Black lines are the fit and the dashed vertical lines show the thresholds of respectively: (red) 1%, (blue) 5%, and (light blue) 10%.

same time preserving real ones in other samples. With this threshold, the percentage of O<sub>3</sub> detections that are filtered in the whole data set is about 80%, while the percentage of O<sub>3</sub> detections filtered out in the perihelion season (180° < Ls < 340°) is 93%. A detailed view of the impact of the DoF criterion can be found in Supporting Information S1.

### 3.6.4. Ozone $\Delta\chi^2$

The  $\Delta\chi^2$  criterion has been introduced to allow for a rational way to discriminate meaningful fits from spurious detections of ozone. This criterion is defined as the ratio of the residual root mean square ( $\chi^2$ ) obtained when fitting the transmittances without considering O<sub>3</sub> and the  $\chi^2$  of the fit when including the O<sub>3</sub> contribution:

$$\Delta\chi^2 = \frac{\chi^2(\text{no O}_3)}{\chi^2(\text{O}_3)} \quad (7)$$

Residual root mean square values are calculated for each transmittance, that is, at each tangent height  $z_{tg}$ , using the following expression:

$$\chi^2(z_{tg}) = \frac{\sum [w_i \times (y_{fit_i} - y_{obs_i})^2]}{\sum w_i} \quad (8)$$

with  $i = 1, \dots, N$ , with  $N$  is the number of points (wavelengths) and  $w_i$  is the weight defined by  $1/\epsilon_i^2$ .  $\epsilon_i$  is the error on  $y_{fit_i}$ , calculated using the results of the fit (i.e., ozone abundance, polynomial representing the background, or dust optical depth and Ångström coefficient, depending on the method used). In ASIMUT (i.e., FOEM and DOP methods), the errors on the calculated transmittances  $\epsilon_i$  are derived using the Rodgers formalism (Rodgers, 2000):

$$\epsilon = \sqrt{\mathbf{KSK}^T} f(x) \quad (9)$$

Where  $x$  is the state vector (the fitted parameters),  $f(x)$  represent the forward model (here also noted as  $y_{fit}$ ),  $\mathbf{K}$  is the Jacobian matrix  $\mathbf{K} = \partial f/\partial x$  and  $\mathbf{S}$  is the error matrix:

$$\mathbf{S} = (\mathbf{S}_a^{-1} + \mathbf{K}^T \mathbf{S}_e^{-1} \mathbf{K})^{-1} \quad (10)$$

where  $\mathbf{S}_a$  is the a priori covariance matrix representing the variability of the variable considered and  $\mathbf{S}_e$  is the error covariance matrix of the measurements.

A value of  $\Delta\chi^2 < 1$  means the fit is better without O<sub>3</sub> than with O<sub>3</sub>, thus we will not retain the ozone detection. Following an approach similar to Määttä et al. (2022), we computed a threshold for each retrieval method - FOEM, DOP, and OP: we only accept O<sub>3</sub> detections whose  $\Delta\chi^2$  is above such threshold.

To derive the  $\Delta\chi^2$  thresholds, we proceeded as for the DoF criterion, and we used the same sample of occultations without O<sub>3</sub> (null-test set). We therefore derived a distribution for each retrieval method, as displayed in Figure 8. We fitted a  $\chi^2$  distribution to the three cases, considering only  $\Delta\chi^2 \geq 1$ , and O<sub>3</sub> values >DL. We opted for a threshold of 10% for the three methods (see Table 1), which means that a  $\Delta\chi^2 >$  the threshold has 10% probability to be a spurious detection within the null-test sample. The choice of a 10% threshold was done empirically. In Supporting Information S1, Section S1, we present in more detail the impact of different threshold values (10%, 5%, and 1%).

In Figure 4 and Table 1, we present the impact of applying the  $\Delta\chi^2$  criterion: it removes up to 90% of O<sub>3</sub> detections in the whole data set, and up to 98% in the perihelion season (180° < Ls < 340°) (See also Table S2 in Supporting Information S1). This criterion excludes spurious O<sub>3</sub> detections due to instrumental effects, or high dust content. The combination of the DL and the  $\Delta\chi^2$  criteria eliminates ~81% of ozone detections. We note that there is a large discrepancy between the filtered detections for the FOEM and DOP methods (80%–90%) compared to the OP method (36%). A possible explanation could be that the OP method simply does not converge when the information content is too low. On the other hand, the DOP and FOEM methods tend to provide always a solution, that in the case of the FOEM method, is the a priori.

In Figure 5, we present an example of O<sub>3</sub> detection that is filtered out by the DL criterion, but not by the  $\Delta\chi^2 > 1.1$  at 25 km. Figure 9 shows an example of ozone detections filtered out by  $\Delta\chi^2 > 1.1$  criterion but not by the DL criterion at all altitudes for the FOEM profile. The DOP and OP profiles show a better agreement below 45 km and are above the DL. A visual inspection of the spectra does not show a clear presence of ozone. Both examples

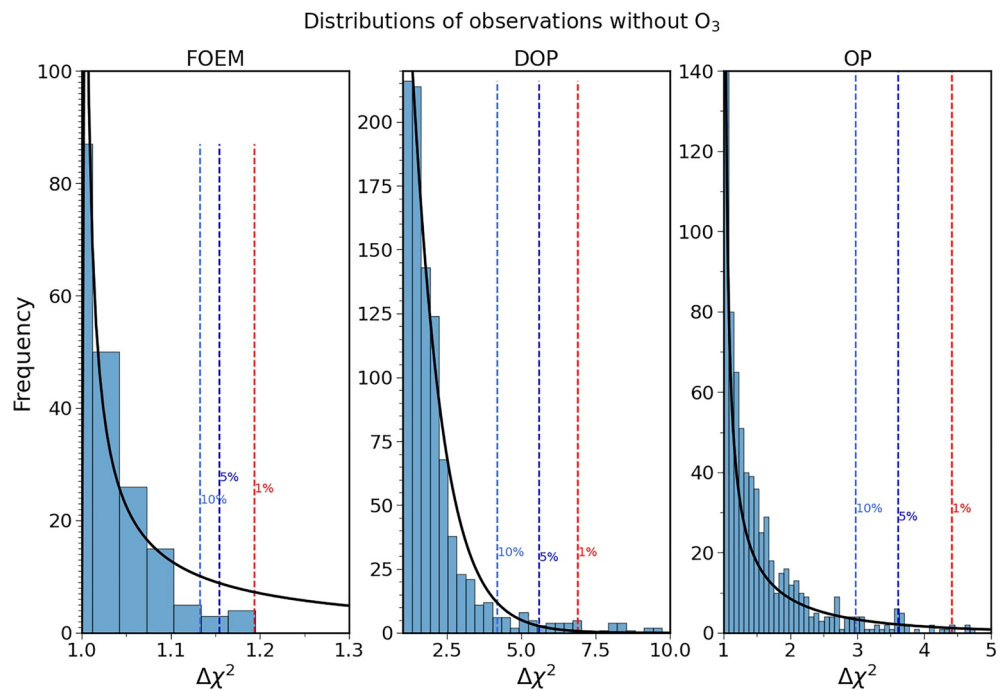


**Figure 8.** Histograms represent the distributions of a sample of occultation without O<sub>3</sub> for the three retrieval methods. Black line are the fit and the dashed vertical lines show the thresholds of respectively: (red) 1%, (blue) 5%, and (light blue) 10%.

(Figures 5 and 9) confirm that more than one filtering criterion is necessary to correctly identify spurious detection of O<sub>3</sub>.

## 4. Retrieval Comparison

### 4.1. Comparison of NOMAD-UVIS Retrievals

We compared the retrievals of ozone obtained by the three different retrieval methods. In the following figures we combined all latitudes together, in order to focus on solar longitude differences. We considered only values of ozone that satisfy the following criteria: (a) O<sub>3</sub> > DL, and (b)  $\Delta\chi^2$  > threshold for the three retrieval methods (see Table 1). Figures 10a and 10b display the percentage differences of vertical profiles of O<sub>3</sub> number density obtained by the three approaches. Most of observations near the perihelion are filtered out, as was expected from the comparison with GEM-Mars GCM (see Figure 6). Near the aphelion season, O<sub>3</sub> profiles extend from about 10 km up to 50–60 km of altitude. The criteria eliminate up to 81% of ozone detections, especially above approximately 50–60 km.

There is generally a good agreement below 50 km, with a maximum percentage difference of ~45% at high altitude. Above this altitude FOEM profiles appear to be slightly below OP and DOP profiles, this is probably due to the dependence of FOEM profiles to their a priori above 50 km. In fact, as can be clearly seen in Figure 3, above 50–60 km, FOEM retrieved profiles tend to converge back to their a priori.

In Figure 10c, we display in blue all ozone retrievals derived with the FOEM method, while ozone values that do not satisfy the filtering criteria are shown in yellow. Comparing FOEM ozone detections filtered out by the above criteria (see yellow dots in Figure 10c) with the aerosols extinction vertical distribution (figure obtained by the OP method), we can observe a clear correlation between high level of aerosols in the atmosphere and spurious detections of O<sub>3</sub> that are filtered out by the criteria.

In the rest of this manuscript, we will use the FOEM results in the figures. Although the three retrieval methods give consistent results, the FOEM method offers additional features, such as the possibility to include gradients in the retrieval, that we would like to apply in a future study.

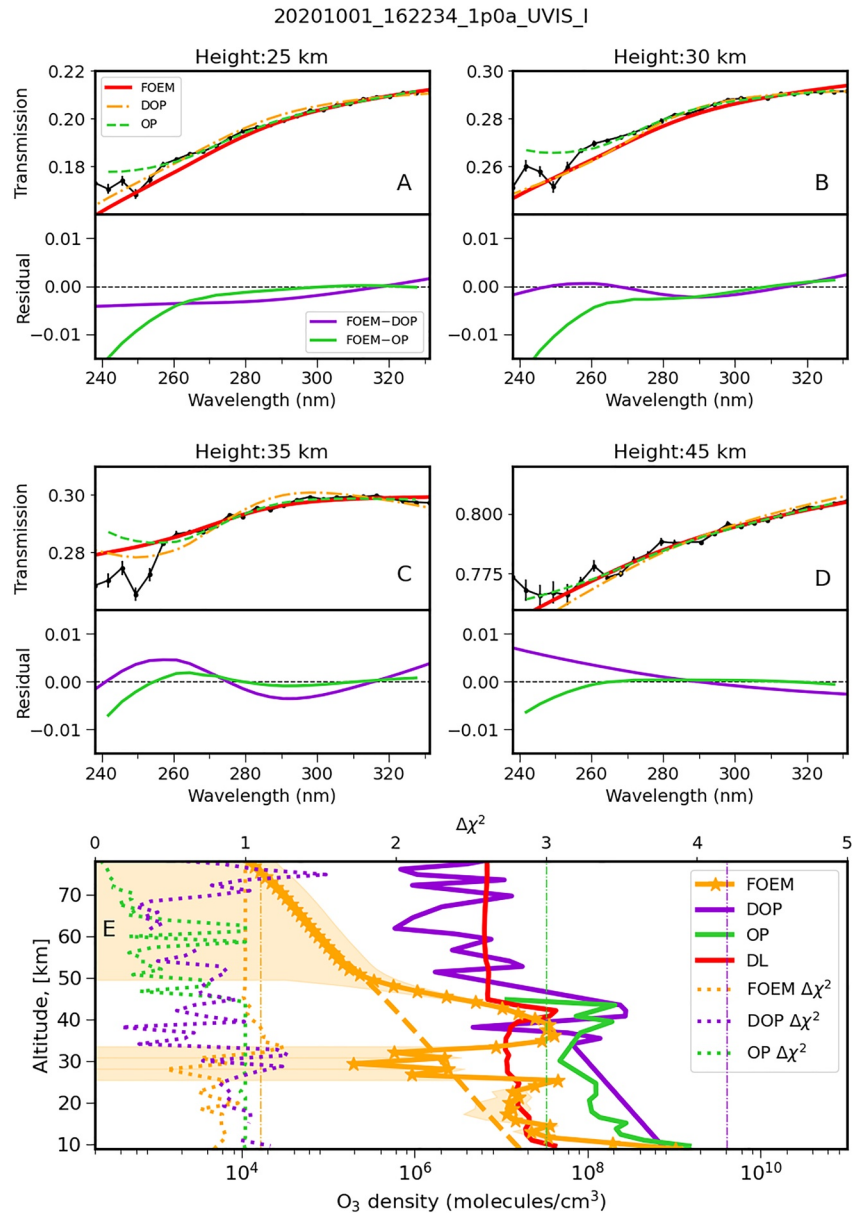


**Figure 9.** (a–d) The top panel shows the spectrum for four different altitudes (black) and the fits for the three retrieval methods. The bottom panel displays the differences between the FOEM method and the DOP and OP methods (violet and green curves, respectively). (e) Retrieved ozone profiles (solid lines) with the FOEM (yellow), DOP (purple), and OP (green) methods. The dashed yellow line is the a priori. We displayed the DL as a red line. The  $\Delta\chi^2$  values and their thresholds (dash-dotted lines) are also shown for the three methods.

Figure 10e displays ozone concentrations as function of solar longitude ( $L_s$ ) and altitude obtained with the FOEM method after filtering. In Supporting Information S1, we compared our retrievals to the NOMAD-UVIS ozone data set (OU) derived by Patel, Mason, et al. (2021); Patel, Sellers, et al. (2021).

#### 4.2. Comparison of Filtering Methods Between UVIS and SPICAM

Spectroscopie pour l'Investigation des Caractéristiques Atmosphériques de Mars (SPICAM) is a UV and IR spectrometer that has been observing the Martian atmosphere since 2004 on the Mars Express satellite (Bertaux et al., 2006; Montmessin et al., 2017). SPICAM measured ozone on Mars with its UV channel that operated from 2004 until 2014. This channel ranges from 118 to 320 nm and detects the ozone Hartley band centered

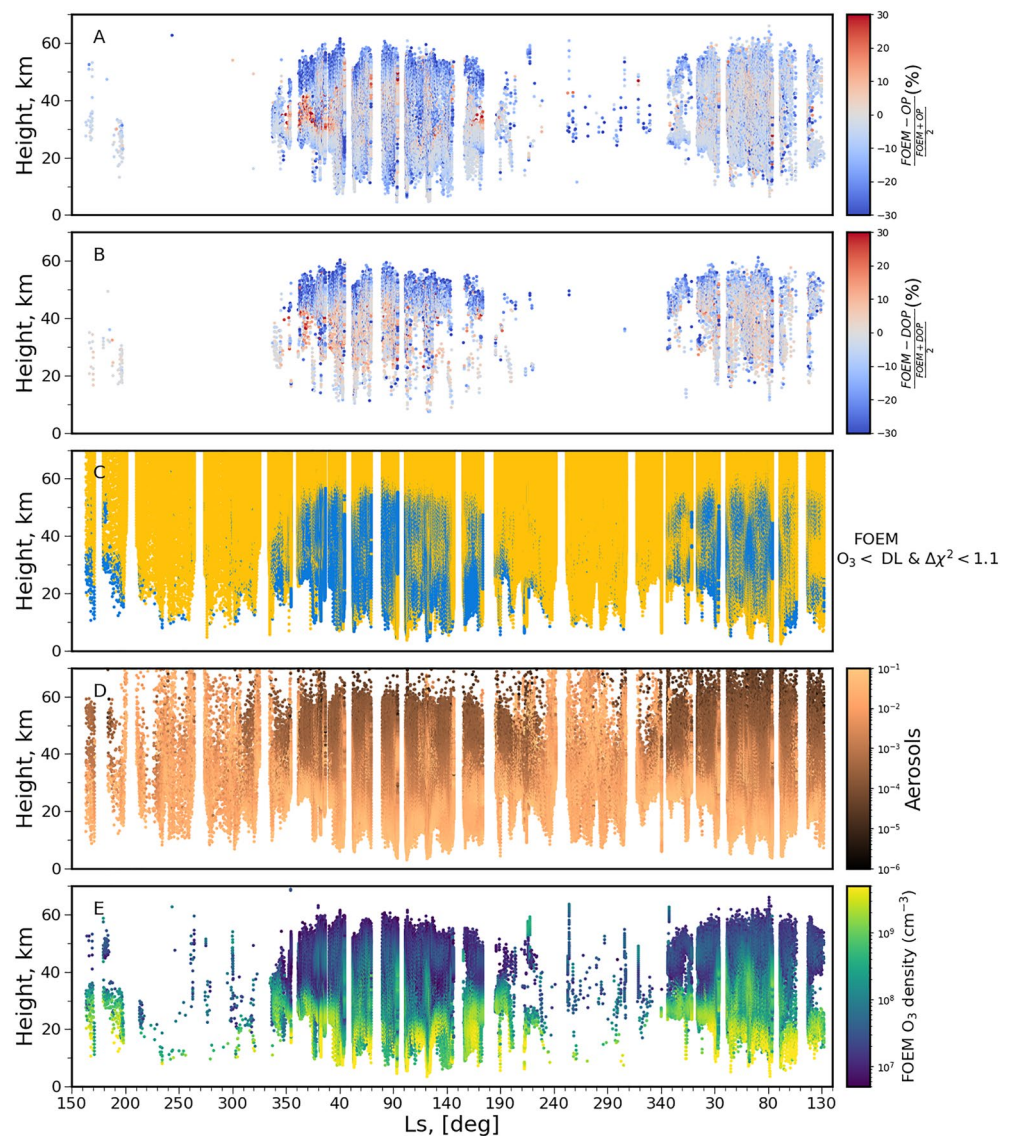


**Figure 10.** From top to bottom: (a) Percentage differences of vertical profiles of  $O_3$  number density obtained by the FOEM and the OP methods; (b) Percentage differences of vertical profiles of  $O_3$  number density obtained by the FOEM and by the DOP methods; (c) In blue are shown all ozone retrievals derived with the FOEM method, in yellow ozone values that do not satisfy the filtering criteria:  $O_3 < DL$  and  $\Delta\chi^2 < 1.1$ ; (d) Aerosols extinction vertical distribution ( $cm^{-1}$ ) obtained by the OP method; (e) Ozone vertical distribution ( $cm^{-3}$ ) derived with the FOEM method.

around 255 nm. SPICAM data have been used to produce ozone column retrievals (Lefèvre et al., 2021; Perrier et al., 2006; Willame et al., 2017) and vertical profiles from stellar occultations (Lebonnois et al., 2006; Montmessin & Lefèvre, 2013). Recently, the SPICAM team published a new ozone vertical distribution data set combining SPICAM stellar and solar occultations in the UV (Määttä et al., 2022).

The occultation retrievals are performed through a classical method combining a spectral inversion through fitting the Beer-Lambert law to the transmissions and a vertical inversion through the onion-peeling method (see, e.g., Määttä et al. (2013)). The ozone retrievals have proven to be more complex than expected, and several reasons led to spurious ozone detections when using only the previously mentioned classical retrieval method. Such detections were caused by remaining systematics in the data, influence of aerosols, and the fitting method (Levenberg-Marquardt) converging on local minima. The spurious detections were very prominent especially above 10–20 km during the second half of the year when only very low amounts of ozone are expected at these altitudes. The SPICAM team has now developed an additional method for filtering these spurious detections

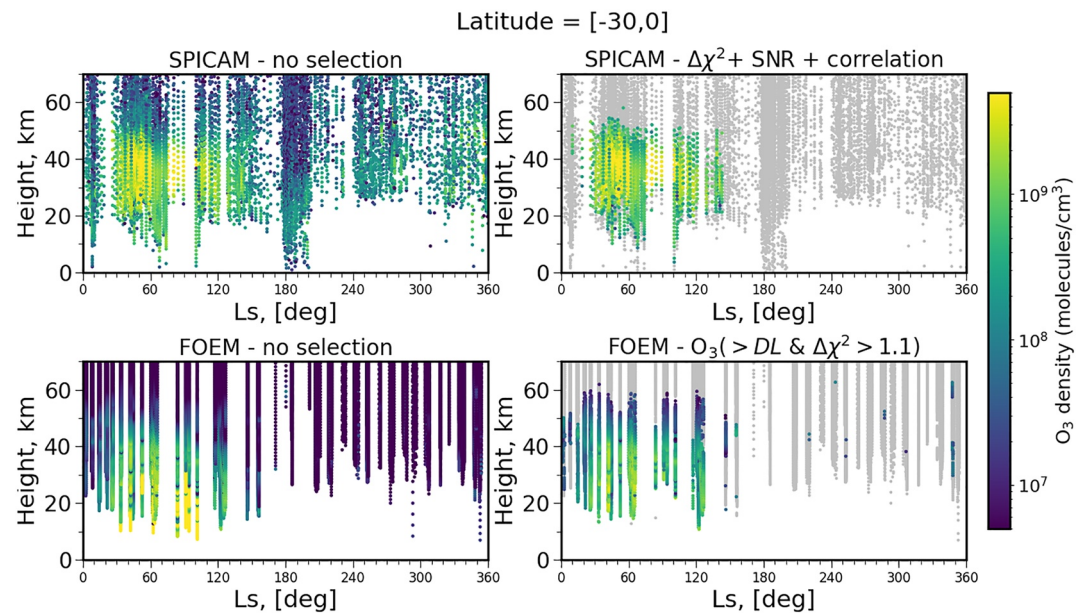


**Figure 11.** An example of the effect of the selection criteria for SPICAM-UV and NOMAD-UVIS observations (FOEM method) for a latitude band ( $-30^{\circ}$ ,  $0^{\circ}$ ). We showed both SPICAM stellar and solar occultations. Left panels show the ozone vertical distribution before applying the filtering; right panels shows  $O_3$  profiles after the selection criteria.

(Määttänen et al., 2022). The criteria used for filtering their data are similar to the ones adopted here, in particular concerning the  $\Delta\chi^2$  criterion. Their additional criteria are the signal-to-noise ratio and a correlation coefficient. The latter is a Pearson's correlation coefficient calculated between the data and the model, both normalized to exclude aerosol signature (see Määttänen et al. (2022) for details).

In Figure 11 we compare the results of the filtering methods for a latitude band ( $-30^{\circ}$ ,  $0^{\circ}$ ) for SPICAM and UVIS data. It should be kept in mind that in the figures we combined SPICAM stellar and solar occultations, therefore, the absolute values should not be compared as the local times are different and ozone is much more abundant during the night. Moreover, the two instruments did not observe during the same Mars Years. As a reminder, SPICAM observed in MYs 27–30, while NOMAD during MYs 34–36. Nevertheless, both filtering techniques led to very similar results, most of the ozone detections during the second half of the year and above approximately 50 km throughout the year being discarded. However, at perihelion some ozone detections are still present in the NOMAD data set, while these are completely filtered out in the SPICAM data set. There may be various explanations for this, such as different filtering criteria, different spectral ranges or a different choice of the null-test sample. Additional comparisons between SPICAM and UVIS at different latitudes can be found Supporting Information S1. These results reveal that retrieving ozone from occultation measurements is not a straightforward task: it is very sensitive to the data quality and the fitting methods, and our example shows that it is a problem shared by two different instruments. This points to a need to evaluate carefully the quality of retrievals for detection of ozone in occultations in particular, and of trace gases in general.

## 5. Conclusions

We have here presented an inter-comparison of retrieval codes for ozone observed with the NOMAD-UVIS instrument on board ExoMars TGO. We analyzed almost two Martian years of observations, corresponding to more than 8,300 solar occultations, acquired between April 2018 (MY 34,  $L_s = 163^{\circ}$ ) and November 2021 (MY 36,  $L_s = 132^{\circ}$ ).

As in the work of Määttänen et al. (2022) for SPICAM-UV occultations, the NOMAD-UVIS ozone retrievals proved to be more difficult than expected due to the presence of spurious  $O_3$  detections. We therefore decided to test different retrieval approaches.



We used three retrieval codes: (a) an onion peeling method (OP), (b) a full occultation Optimal Estimation Method (FOEM), and (c) a direct onion peeling method (DOP), introduced here for the first time. The three retrieval methods produce consistent results, especially where ozone densities are higher.

The main challenge was to find reliable criteria to identify the spurious detections of O<sub>3</sub> caused by instrumental effects, high dust content, or very low ozone quantities. We evaluated the impact of different filtering criteria for the three retrieval approaches and we finally adopted two criteria for filtering the data: (a) a detection limit (DL), and (b) the  $\Delta\chi^2$  criterion. The DL criterion excludes very low values of O<sub>3</sub> that do not have physical meaning. The  $\Delta\chi^2$  criterion eliminates very high values of ozone, that is spurious detections, mainly produced by instrumental effects, or high aerosol content. Both criteria filter out 81% of detections, especially O<sub>3</sub> values near the perihelion, where, based also on simulations from the GEM-Mars GCM (Daerden, Neary, Villanueva, et al., 2022; Daerden, Neary, Wolff, et al., 2022), we expected low values of ozone, and above about 50 km.

After filtering (See Figure 4), our results confirm the main features observed by earlier studies on the NOMAD-UVIS data set (Khayat et al., 2021; Patel, Mason, et al., 2021; Patel, Sellers, et al., 2021). In particular, (a) the high-altitude ozone peak between 40 and 60 km in the Northern hemisphere, visible during mid-northern spring, late northern summer-early southern spring, and late southern summer, and (b) a second peak, visible in the South at polar latitudes.

We compared the results of filtering with SPICAM-UV observations. The SPICAM team applied very similar criteria for filtering their data to the ones implemented here. Even if the two instruments did not observe during the same Martian Years both filtering approaches led to very similar results.

Remote sensing of planetary atmospheres represents the most efficient way to constrain their composition, thermal structure, and aerosols coverage (Irwin et al., 2008). Multiple retrievals methods, and various approaches to error estimation, can be used on observations from remote sensing instruments. While the choice of a specific method may depend on different factors and each retrieval code may be particularly suited for a specific task, it is extremely important to ensure consistency between different retrieval schemes. This is not a straightforward task: the retrieval of ozone, and more generally of trace gases, is very sensitive to data quality and to the fitting methods. There is therefore a need to evaluate with attention the quality of retrievals of trace gases for the planetary atmospheres within our own Solar System and beyond.

## Data Availability Statement

Public access to all ExoMars TGO data are available through the ESA Planetary Science Archive ([archives.esac.esa.int/psa/](https://archives.esac.esa.int/psa/)) with additional access to NOMAD data through the PI institute ([nomad.aeronomie.be](https://nomad.aeronomie.be)). The results retrieved from the NOMAD measurements used in this article are available on the BIRA-IASB data repository: <https://repository.aeronomie.be/?doi=10.18758/71021079> (Piccialli & Vandaele, 2022).

## References

- Barth, C. A., & Hord, C. W. (1971). Mariner ultraviolet spectrometer: Topography and polar cap. *Science*, 173(3993), 197–201. <https://doi.org/10.1126/science.173.3993.197>
- Barth, C. A., Hord, C. W., Stewart, A. I., Lane, A. L., Dick, M. L., & Anderson, G. P. (1973). Mariner 9 ultraviolet spectrometer experiment: Seasonal variation of ozone on Mars. *Science*, 179(4075), 795–796. <https://doi.org/10.1126/science.179.4075.795>
- Bertaux, J.-L., Korabiev, O., Perrier, S., Quémerais, E., Montmessin, F., Leblanc, F., et al. (2006). SPICAM on Mars Express: Observing modes and overview of UV spectrometer data and scientific results. *Journal of Geophysical Research: Planets*, 111(E10), E10S90. <https://doi.org/10.1029/2006JE002690>
- Brion, J., Chakir, A., Daumont, D., Malicet, J., & Parisse, C. (1993). High-resolution laboratory absorption cross section of O<sub>3</sub>. Temperature effect. *Chemical Physics Letters*, 213(5–6), 610–612. [https://doi.org/10.1016/0009-2614\(93\)89169-I](https://doi.org/10.1016/0009-2614(93)89169-I)
- Clancy, R. T., Grossman, A. W., Wolff, M. J., James, P. B., Rudy, D. J., Billawala, Y. N., et al. (1996). Water vapor saturation at low altitudes around Mars aphelion: A key to Mars climate? *Icarus*, 122(1), 36–62. <https://doi.org/10.1006/icar.1996.0108>
- Clancy, R. T., Smith, M. D., Lefèvre, F., McConnochie, T. H., Sandor, B. J., Wolff, M. J., et al. (2017). Vertical profiles of Mars 1.27  $\mu\text{m}$  O<sub>2</sub> dayglow from MRO CRISM limb spectra: Seasonal/global behaviors, comparisons to LMDGCM simulations, and a global definition for Mars water vapor profiles. *Icarus*, 293, 132–156. <https://doi.org/10.1016/j.icarus.2017.04.011>
- Clancy, R. T., Wolff, M. J., & James, P. B. (1999). Minimal aerosol loading and global increases in atmospheric ozone during the 1996–1997 Martian northern spring season. *Icarus*, 138(1), 49–63. <https://doi.org/10.1006/icar.1998.6059>
- Daerden, F., Neary, L., Villanueva, G., Liuzzi, G., Aoki, S., Clancy, R. T., et al. (2022). Explaining nomad d/h observations by cloud-induced fractionation of water vapor on Mars. *Journal of Geophysical Research: Planets*, 127(2), e2021JE007079. <https://doi.org/10.1029/2021JE007079>
- Daerden, F., Neary, L., Viscardi, S., García Muñoz, A., Clancy, R. T., Smith, M. D., et al. (2019). Mars atmospheric chemistry simulations with the GEM-Mars general circulation model. *Icarus*, 326, 197–224. <https://doi.org/10.1016/j.icarus.2019.02.030>

## Acknowledgments

The NOMAD experiment is led by the Royal Belgian Institute for Space Aeronomy (IASB-BIRA), with Co-PI teams in the United Kingdom (Open University), Spain (IAA-CSIC) and Italy (INAF-IAPS). This project has received funding from the European Union's Horizon 2020 research and innovation programme under Grant agreement No 101004052. This work was supported by the NASA's Mars Program Office under WBS 604796, "Participation in the TGO/NOMAD Investigation of Trace Gases on Mars." The material was based upon the work supported by the NASA under award No. 80GSFC21M0002. The authors acknowledge funding from the UK Space Agency through Grants ST/V002295/1, ST/V005332/1, and ST/S00145X/1. AM acknowledges the support from the French Space Agency CNES. JJLM acknowledges financial support from the State Agency for Research of the Spanish MCIU through the "Center of Excellence Severo Ochoa" award to the Instituto de Astrofísica de Andalucía (SEV-2017-0709) and by Grant PGC2018-101836-B-I00 funded by MCIU/AEI/10.13039/501100011033 and by "ERDF A way of making Europe."

- Daerden, F., Neary, L., Wolff, M. J., Clancy, R. T., Lefèvre, F., Whiteway, J. A., et al. (2022). Planet-wide ozone destruction in the middle atmosphere on Mars during global dust storm. *Geophysical Research Letters*, *49*(11), e2022GL098821. <https://doi.org/10.1029/2022GL098821>
- Daumont, D., Brion, J., Charbonnier, J., & Malicet, J. (1992). Ozone UV spectroscopy. I - absorption cross-sections at room temperature. *Journal of Atmospheric Chemistry*, *15*(2), 145–155. <https://doi.org/10.1007/BF00053756>
- Dubovik, O., Smirnov, A., Holben, B. N., King, M. D., Kaufman, Y. J., Eck, T. F., & Slutsker, I. (2000). Accuracy assessments of aerosol optical properties retrieved from Aerosol Robotic Network (AERONET) Sun and sky radiance measurements. *Journal of Geophysical Research*, *105*(D8), 9791–9806. <https://doi.org/10.1029/2000JD900040>
- Fast, K., Kostiuk, T., Espenak, F., Annen, J., Buhl, D., Hewagama, T., et al. (2006). Ozone abundance on Mars from infrared heterodyne spectra. I. Acquisition, retrieval, and anticorrelation with water vapor. *Icarus*, *181*(2), 419–431. <https://doi.org/10.1016/j.icarus.2005.12.001>
- Gröller, H., Montmessin, F., Yelle, R. V., Lefèvre, F., Forget, F., Schneider, N. M., et al. (2018). MAVEN/IUVS stellar occultation measurements of Mars atmospheric structure and composition. *Journal of Geophysical Research: Planets*, *123*(6), 1449–1483. <https://doi.org/10.1029/2017JE005466>
- Huestis, D. L., & Berkowitz, J. (2010). Critical evaluation of the photoabsorption cross section of CO<sub>2</sub> from 0.125 to 201.6 nm at R<sub>o,m</sub> temperature. In *Aas/division for planetary sciences meeting abstracts #42* (Vol. 42, p. 48.13).
- Irwin, P. G. J., Teanby, N. A., de Kok, R., Fletcher, L. N., Howett, C. J. A., Tsang, C. C. C., et al. (2008). The NEMESIS planetary atmosphere radiative transfer and retrieval tool. *Journal of Quantitative Spectroscopy and Radiative Transfer*, *109*(6), 1136–1150. <https://doi.org/10.1016/j.jqsrt.2007.11.006>
- Khayat, A. S. J., Smith, M. D., Wolff, M., Daerden, F., Neary, L., Patel, M. R., et al. (2021). ExoMars TGO/NOMAD-UVIS vertical profiles of ozone: 2. The high-altitude layers of atmospheric ozone. *Journal of Geophysical Research: Planets*, *126*(11), e06834. <https://doi.org/10.1029/2021JE006834>
- Lebonnois, S., Quémerais, E., Montmessin, F., Lefèvre, F., Perrier, S., Bertaux, J.-L., & Forget, F. (2006). Vertical distribution of ozone on Mars as measured by SPICAM/Mars Express using stellar occultations. *Journal of Geophysical Research*, *111*(E9), E09S05. <https://doi.org/10.1029/2005JE002643>
- Lefèvre, F., Trokhimovskiy, A., Fedorova, A., Baggio, L., Lacombe, G., Määttänen, A., et al. (2021). Relationship between the ozone and water vapor columns on Mars as observed by SPICAM and calculated by a global climate model. *Journal of Geophysical Research: Planets*, *126*(4), e06838. <https://doi.org/10.1029/2021JE006838>
- Määttänen, A., Lefèvre, F., Verdier, L., Montmessin, F., Listowski, C., Guilbon, S., et al. (2022). Ozone vertical distribution in Mars years 27–30 from SPICAM/MEX UV occultations. *Icarus*, *387*, 115162. <https://doi.org/10.1016/j.icarus.2022.115162>
- Määttänen, A., Listowski, C., Montmessin, F., Maltagliati, L., Reberac, A., Joly, L., & Bertaux, J.-L. (2013). A complete climatology of the aerosol vertical distribution on Mars from MEX/SPICAM UV solar occultations. *Icarus*, *223*(2), 892–941. <https://doi.org/10.1016/j.icarus.2012.12.001>
- Malicet, J., Daumont, D., Charbonnier, J., Parisse, C., Chakir, A., & Brion, J. (1995). Ozone UV spectroscopy. II. Absorption cross-sections and temperature dependence. *Journal of Atmospheric Chemistry*, *21*(3), 263–273. <https://doi.org/10.1007/BF00696758>
- Mason, J. P., Patel, M. R., Leese, M. R., Hathi, B. G., Willame, Y., Thomas, I. R., et al. (2022). Removal of straylight from exomars NOMAD-UVIS observations. *Planetary and Space Science*, *218*, 105432. <https://doi.org/10.1016/j.pss.2022.105432>
- Montabone, L., Forget, F., Millour, E., Wilson, R., Lewis, S., Cantor, B., et al. (2015). Eight-year climatology of dust optical depth on Mars. *Icarus*, *251*, 65–95. <https://doi.org/10.1016/j.icarus.2014.12.034>
- Montabone, L., Spiga, A., Kass, D. M., Kleinböhl, A., Forget, F., & Millour, E. (2020). Martian year 34 column dust climatology from Mars climate sounder observations: Reconstructed maps and model simulations. *Journal of Geophysical Research: Planets*, *125*(8), e2019JE006111. <https://doi.org/10.1029/2019JE006111>
- Montmessin, F., Bertaux, J. L., Lefèvre, F., Marcq, E., Belyaev, D., Gérard, J. C., et al. (2011). A layer of ozone detected in the nightside upper atmosphere of Venus. *Icarus*, *216*(1), 82–85. <https://doi.org/10.1016/j.icarus.2011.08.010>
- Montmessin, F., Bertaux, J.-L., Quémerais, E., Korablev, O., Rannou, P., Forget, F., et al. (2006). Subvisible CO<sub>2</sub> ice clouds detected in the mesosphere of Mars. *Icarus*, *183*(2), 403–410. <https://doi.org/10.1016/j.icarus.2006.03.015>
- Montmessin, F., Korablev, O., Lefèvre, F., Bertaux, J. L., Fedorova, A., Trokhimovskiy, A., et al. (2017). SPICAM on Mars express: A 10 year in-depth survey of the Martian atmosphere. *Icarus*, *297*, 195–216. <https://doi.org/10.1016/j.icarus.2017.06.022>
- Montmessin, F., & Lefèvre, F. (2013). Transport-driven formation of a polar ozone layer on Mars. *Nature Geoscience*, *6*(11), 930–933. <https://doi.org/10.1038/ngeo1957>
- Neefs, E., Vandaele, A. C., Drummond, R., Thomas, I. R., Berkenbosch, S., Clairquin, R., et al. (2015). NOMAD spectrometer on the ExoMars trace gas orbiter mission: Part 1—Design, manufacturing and testing of the infrared channels. *Applied Optics*, *54*(28), 8494. <https://doi.org/10.1364/AO.54.008494>
- Olsen, K. S., Fedorova, A. A., Trokhimovskiy, A., Montmessin, F., Lefèvre, F., Korablev, O., et al. (2022). Seasonal changes in the vertical structure of ozone in the Martian lower atmosphere and its relationship to water vapour. *Journal of Geophysical Research: Planets*, *127*(10), e2022JE007213. <https://doi.org/10.1029/2022JE007213>
- Parkinson, W. H., Rufus, J., & Yoshino, K. (2003). Absolute absorption cross section measurements of CO<sub>2</sub> in the wavelength region 163–200 nm and the temperature dependence. *Chemical Physics*, *290*(2–3), 251–256. [https://doi.org/10.1016/S0301-0104\(03\)00146-0](https://doi.org/10.1016/S0301-0104(03)00146-0)
- Patel, M., Mason, J., Sellers, G., & Holmes, J. (2021). *Nomad-UVIS ozone vertical profile retrievals for mars year 34-35*. The Open University. <https://doi.org/10.21954/ou.rd.13580336.v1>
- Patel, M. R., Antoine, P., Mason, J., Leese, M., Hathi, B., Stevens, A. H., et al. (2017). NOMAD spectrometer on the ExoMars trace gas orbiter mission: Part 2—Design, manufacturing, and testing of the ultraviolet and visible channel. *Applied Optics*, *56*(10), 2771. <https://doi.org/10.1364/ao.56.002771>
- Patel, M. R., Sellers, G., Mason, J. P., Holmes, J. A., Brown, M. A. J., Lewis, S. R., et al. (2021). ExoMars TGO/NOMAD-UVIS vertical profiles of ozone: 1. Seasonal variation and comparison to water. *Journal of Geophysical Research: Planets*, *126*(11), e06837. <https://doi.org/10.1029/2021JE006837>
- Perrier, S., Bertaux, J. L., Lefèvre, F., Lebonnois, S., Korablev, O., Fedorova, A., & Montmessin, F. (2006). Global distribution of total ozone on Mars from SPICAM/MEX UV measurements. *Journal of Geophysical Research*, *111*(E9), E09S06. <https://doi.org/10.1029/2006JE002681>
- Piccialli, A., Montmessin, F., Belyaev, D., Mahieux, A., Fedorova, A., Marcq, E., et al. (2015). Thermal structure of Venus nightside upper atmosphere measured by stellar occultations with SPICAV/Venus Express. *Planetary and Space Science*, *113*, 321–335. <https://doi.org/10.1016/j.pss.2014.12.009>
- Piccialli, A., & Vandaele, A. C. (2022). Global distribution of ozone vertical profiles retrieved from nomad-uviss/tgo, presented in piccialli et al. 2022 [Dataset]. (BIRAIASB). <https://doi.org/10.18758/71021079>
- Piccialli, A., Vandaele, A. C., Trompet, L., Neary, L., Viscardy, S., Erwin, J. T., et al. (2021). Impact of gradients at the Martian terminator on the retrieval of ozone from SPICAM/MEX. *Icarus*, *353*, 113598. <https://doi.org/10.1016/j.icarus.2019.113598>

- Quémerais, E., Bertaux, J.-L., Korabev, O., Dimarellis, E., Cot, C., Sandel, B. R., & Fussen, D. (2006). Stellar occultations observed by SPICAM on Mars Express. *Journal of Geophysical Research*, *111*(E9), 9. <https://doi.org/10.1029/2005JE002604>
- Rodgers, C. D. (2000). Inverse methods for atmospheric sounding: Theory and practice. <https://doi.org/10.1142/3171>
- Sander, S. P., Abbatt, J., Barker, J., Burkholder, J., Friedl, R., Golden, D., et al. (2011). Chemical kinetics and photochemical data for use in atmospheric studies [Evaluation No. 17].
- Serdyuchenko, A., Gorshlev, V., Weber, M., Chegade, W., & Burrows, J. P. (2014). High spectral resolution ozone absorption cross-sections - Part 2: Temperature dependence. *Atmospheric Measurement Techniques*, *7*(2), 625–636. <https://doi.org/10.5194/amt-7-625-2014>
- Trompet, L., Mahieux, A., Ristic, B., Robert, S., Wilquet, V., Thomas, I. R., et al. (2016). Improved algorithm for the transmittance estimation of spectra obtained with SOIR/Venus Express. *Applied Optics*, *55*(32), 9275. <https://doi.org/10.1364/AO.55.009275>
- Trompet, L., Robert, S., Mahieux, A., Schmidt, F., Erwin, J., & Vandaele, A. C. (2021). Phosphine in Venus' atmosphere: Detection attempts and upper limits above the cloud top assessed from the SOIR/VEx spectra. *Astronomy & Astrophysics*, *645*, L4. <https://doi.org/10.1051/0004-6361/202039932>
- Trompet, L., Vandaele, A. C., Thomas, I., Aoki, S., Daerden, F., Erwin, J., et al. (2023). Carbon dioxide retrievals from NOMAD-SO on ESA's ExoMars Trace Gas Orbiter and temperature profiles retrievals with the hydrostatic equilibrium equation. I. Description of the method. *Journal of Geophysical Research: Planets*. <https://doi.org/10.1029/2022JE007277>
- Vandaele, A. C., De Mazière, M., Drummond, R., Mahieux, A., Neefs, E., Wilquet, V., et al. (2008). Composition of the Venus mesosphere measured by solar occultation at infrared on board Venus express. *Journal of Geophysical Research*, *113*, E00B23. <https://doi.org/10.1029/2008JE003140>
- Vandaele, A. C., Kruglanski, M., & de Mazière, M. (2006). Modeling and Retrieval of atmospheric spectra using ASIMUT. In *Atmospheric science conference* (Vol. 628, p. 71).
- Vandaele, A. C., Lopez-Moreno, J. J., Patel, M. R., Bellucci, G., Daerden, F., Ristic, B., et al. (2018). NOMAD, an integrated suite of three spectrometers for the ExoMars trace gas mission: Technical description, science objectives and expected performance. *Space Science Review*, *214*(5), 80. <https://doi.org/10.1007/s11214-018-0517-2>
- Vandaele, A. C., Neefs, E., Drummond, R., Thomas, I. R., Daerden, F., Lopez-Moreno, J. J., et al. (2015). Science objectives and performances of NOMAD, a spectrometer suite for the ExoMars TGO mission. *Planetary and Space Science*, *119*, 233–249. <https://doi.org/10.1016/j.pss.2015.10.003>
- Willame, Y., Depiesse, C., Mason, J., Thomas, I., Patel, M., Hathi, B., et al. (2022). Calibration of the nomad-UVIS data. *Planetary and Space Science*, *105504*, 105504. <https://doi.org/10.1016/j.pss.2022.105504>
- Willame, Y., Vandaele, A. C., Depiesse, C., Lefèvre, F., Letocart, V., Gillotay, D., & Montmessin, F. (2017). Retrieving cloud, dust and ozone abundances in the Martian atmosphere using SPICAM/UV nadir spectra. *Planetary and Space Science*, *142*, 9–25. <https://doi.org/10.1016/j.pss.2017.04.011>